


Complete miscibility amongst the AV_3Sb_5 kagome superconductors: Design of mixed A-site AV_3Sb_5 (A: K, Rb, Cs) alloys

Brenden R. Ortiz,^{*} Andrea N. Capa Salinas[✉], Miles J. Knudtson, Paul M. Sarte, Ganesh Pokahrel, and Stephen D. Wilson[†]
Materials Department, University of California Santa Barbara, Santa Barbara, California 93106, USA

 (Received 8 November 2022; accepted 23 December 2022; published 6 January 2023)

In this paper, we explore the chemical-property phase diagram of the AV_3Sb_5 family through A-site alloying. We demonstrate full miscibility of the alkali site, highlighting that the three parent compounds are the terminal ends of a single solid solution. Using both polycrystalline and single crystal methods, we map the dependence of the two primary electronic instabilities: (1) the onset of charge-density wave (CDW) order (T_{CDW}) and (2) the onset of superconductivity (T_c) with alkali-site composition. We show continuous trends in both T_{CDW} and T_c , including a region of enhanced CDW stability in $K_{1-x}Cs_xV_3Sb_5$ alloys. Together, our results open new routes for chemical perturbation and exploration of the chemical-property relationships in the class of AV_3Sb_5 kagome superconductors.

DOI: [10.1103/PhysRevMaterials.7.014801](https://doi.org/10.1103/PhysRevMaterials.7.014801)

I. INTRODUCTION

The recent discovery of the AV_3Sb_5 (A: K, Rb, Cs) kagome superconductors [1,2] (Fig. 1) highlights some of the unique possibilities present in kagome metals. The interplay between the emergence of a charge-density wave state (T_{CDW} : 84, 104, and 94 K) [2–4] and superconductivity (T_c : 1.0, 0.8, and 2.5 K) [2–4] in these compounds has generated considerable research into the AV_3Sb_5 family. Underlying this interest are hints of exotic properties ranging from pair density wave superconductivity [5,6], orbital magnetism (chiral charge-density wave) [7–11], and topological surface states [12–14] present in the superconducting phase.

Due in part to its ease of growth, relatively higher T_c , and higher quality crystals, CsV_3Sb_5 has been the primary focus of the AV_3Sb_5 family. Curiously, the current literature hints that many features of CsV_3Sb_5 's charge-density wave state are unique to this variant. In the AV_3Sb_5 family, the real component of the CDW manifests as a 2×2 in-plane superlattice. The associated structural distortion results in individual kagome planes adopting either the “star-of-David (SoD)” or “trihexagonal (TrH)” motif [15–17]. Unlike the K- and Rb-based compounds, CsV_3Sb_5 manifests a combination of both distortion types within a mixed CDW state with both $2 \times 2 \times 4$ and $2 \times 2 \times 2$ order possible [18–20]. Furthermore, the emergence of multiple different temperature regimes within the CDW state, and an apparent sensitivity to thermal history (heating rates, hysteresis, and quenching) are, thus far, unique to CsV_3Sb_5 [21,22]. Small quantities of dopants have also driven changes in the dimensionality of the CDW in CsV_3Sb_5 , suggesting a complex interplay of

coexisting or competing CDW instabilities [23]. Differences amongst the other compounds have been noted as well with KV_3Sb_5 being the only compound to apparently lack the $4a_0$ unidirectional stripe charge order observed at the surface in scanning tunneling microscopy studies [24–26].

Of particular note are the various high-pressure and extrinsic doping studies (e.g., Sn [27,28], Ti [29,30], Nb [31], Ta [32], Mo [32], and O [33]), which have highlighted additional differences between the electronic phase diagram of CsV_3Sb_5 and the Rb/K-based variants. CsV_3Sb_5 exhibits a “double-dome” feature in both high-pressure (<10 GPa) and chemical-doping studies, whereas the Rb and K variants appear to show only “single-dome” superconductivity when perturbed [27,28,34–37]. These differences support the notion of a unique starting CDW state in CsV_3Sb_5 , an effect likely driven by subtle structural (e.g., interlayer distances) differences between the alkali-metal planes and the Zintl-like V-Sb networks.

Chemical alloying is a powerful tool for exploring the relationship between alkali-site character and CDW properties in the AV_3Sb_5 system. Alloys among the three variants stand to provide a tool for exploring a crossover between CDW states, helping to elucidate the underlying mechanism. Here we report the formation and properties of the full suite of isoelectronic alloys $(K,Rb,Cs)V_3Sb_5$. We demonstrate full miscibility of the alkali site, highlighting that the entire AV_3Sb_5 family shares a single solid solution. A continuous though nonlinear dependence of the CDW transition on alkali-site character is shown using 45 unique polycrystalline samples, and a potential crossover along the line of $K_{1-x}Cs_xV_3Sb_5$ alloys is noted. Furthermore, we present the means to design and grow single crystal, mixed A-site AV_3Sb_5 alloys, highlighting changes in T_c as well. This paper expands the chemical phase space of the AV_3Sb_5 kagome superconductors, and demonstrates a framework wherein KV_3Sb_5 , RbV_3Sb_5 , and CsV_3Sb_5 are viewed as terminal end points of a single phase diagram.

^{*}ortiz.brendenr@gmail.com

[†]stephendwilson@ucsb.edu

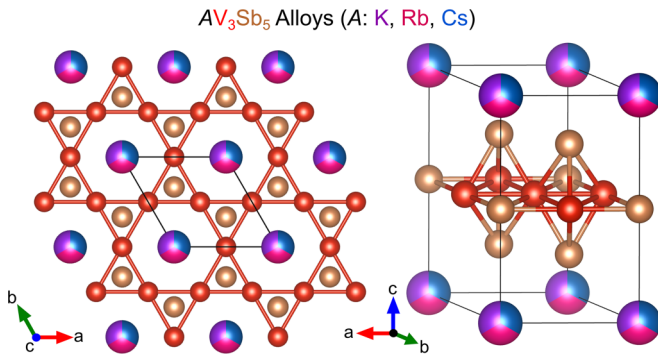


FIG. 1. The AV_3Sb_5 (A: K, Rb, and Cs) kagome superconductors are a family of layered exfoliable kagome metals consisting of a structurally perfect lattice of vanadium at room temperature. All three compounds exhibit a charge-density wave transition and a lower-temperature superconducting ground state. The crystal structure is illustrated above with the alloyed A-site highlighted.

II. EXPERIMENTAL METHODS

A. Polycrystalline synthesis

To generate the large number of polycrystalline AV_3Sb_5 samples desired in this paper, a method similar to that published previously was used [38], appropriately modified for use under inert atmosphere. Amorphous precursor feed stocks with stoichiometric compositions of $A_{1.05}V_3Sb_5$ were created for each of the three parent compounds KV_3Sb_5 , RbV_3Sb_5 , and CsV_3Sb_5 . Elemental K ingot (Alfa Aesar, 99.8%), Rb ingot (Alfa Aesar, 99.75%), Cs liquid (Alfa Aesar, 99.98%), V powder (Sigma-Aldrich, 99.9%), and Sb shot (Alfa Aesar, 99.999%) were sealed into preseasoned tungsten carbide ball mill vials under argon and milled for 90 min in a SPEX 8000D dual mixer/mill. As-received vanadium powder was first purified using a combination of EtOH and concentrated HCl to remove residual oxides on the powder. Resulting feed stocks were then ground and passed through a 100- μ m sieve and stored.

The three feed stock powders were subsequently combined in various ratios to form amorphous AV_3Sb_5 alloy precursors. The mixtures were sealed into 5-ml (SPEX 3127) vials. We subdivided the KV_3Sb_5 – RbV_3Sb_5 – CsV_3Sb_5 phase diagram into 1/8 increments, for a total of 45 unique polycrystalline samples. Vials were sealed under argon and milled for 60 min in batches of eight, utilizing the parallel nature of the SPEX 3127 adapter. The individual (amorphous) mixtures of $(K,Rb,Cs)V_3Sb_5$ were then extracted, ground, and passed through 100- μ m sieves. The powders were sealed in fused silica ampoules under 1 atm of argon and batch annealed at 550 °C for 48 h. Transformed polycrystalline powders were extracted from the ampoules under argon and stored.

Testing for other isoelectronic alloy solubility limits with CsV_3Sb_5 was performed in an analogous way. Feed stocks of hypothetical mixtures corresponding to $CsNb_3Sb_5$, $CsTa_3Sb_5$, NaV_3Sb_5 , CsV_3As_5 , and CsV_3Bi_5 were generated using Nb powder (Alfa Aesar, 99.8%), Ta powder (Alfa Aesar, 99.97%), Na ingot (99.8%), As chunk (Alfa Aesar, 99.9999%), and Bi rod (Alfa Aesar, 99.99%). Alloys were probed by making stoichiometric mixtures of the amorphous precursor phases with

the parent CsV_3Sb_5 precursor phase. We also tested mixtures to confirm that alternate AM_3X_5 phases *do not* form.

B. Single-crystal synthesis

Single-crystal AV_3Sb_5 alloys were grown by a modified self-flux method as performed in prior studies [2,3,18]. Analogous to the polycrystalline study, we synthesized large feed stocks of the parent flux precursors and, subsequently, recombined them to rapidly generate a series of alloyed fluxes. The overall flux composition is slightly modified from prior reports [18] and corresponds to $A_{20}V_{15}Sb_{120}$. Flux feed stocks were produced using the same reagents as the polycrystalline synthesis. The constituent elements were sealed into pre-seasoned tungsten carbide ball mill vials under argon and milled for 90 min in a SPEX 8000D dual mixer/mill.

The three parent feed stocks: $K_{20}V_{15}Sb_{120}$, $Rb_{20}V_{15}Sb_{120}$, and $Cs_{20}V_{15}Sb_{120}$ were then blended to produce the desired $(K,Rb,Cs)_{20}V_{15}Sb_{120}$ flux precursor. Powders were loaded into 2-ml high-density alumina (Coorstek) crucibles and loaded into steel tubes under 1 atm of argon. Samples were heated to 1000 °C at 200 °C/h and, subsequently, soaked at 1000 °C for 12 h. Samples were then cooled relatively quickly to 900 °C at 5 °C/h and then slow cooled to 600 °C at 2 °C/h. Fluxes were cooled completely, and crystals were extracted mechanically. The resulting crystals are thin hexagonal flakes with a metallic silver luster. Typical linear dimensions are 2 mm–1 cm depending on the composition of choice. Crystals are air stable and readily exfoliable.

C. Structural, chemical, and electronic properties characterization

Polycrystalline sample purity and crystallinity was examined with powder x-ray diffraction (XRD) measurements at room temperature on a Panalytical Empyrean diffractometer (Cu $K\alpha_{1,2}$) in Bragg-Brentano (θ - θ) geometry. Rietveld refinement of powder XRD patterns was performed using TOPAS ACADEMIC v6 [39]. Structural models and visualization utilized the VESTA software package [40]. Elemental compositions of both powders and single-crystal samples were measured using a Hitachi TM4000 Plus scanning electron microscope where energy-dispersive spectroscopy (EDS) measurements were performed under an accelerating voltage of 20 kV. Single-crystal samples were exfoliated before measurement.

Magnetization measurements determining the CDW state in AV_3Sb_5 samples were performed using a 7-T Quantum Design magnetic property measurement system superconducting quantum interference device magnetometer in vibrating-sample magnetometry mode. Powders were placed in polypropylene capsules and mounted in a brass sample holder. Single-crystal samples were mounted to quartz holders using GE varnish. Measurements were collected at 1 T under zero-field-cooled conditions.

Electrical resistivity measurements of the superconducting state in single-crystal samples were performed using a Quantum Design 14-T Dynacool physical property measurement systems equipped with a dilution refrigerator insert and the electronic transport option. Single crystals were mounted to

TABLE I. Approximate solubility limits in polycrystalline samples of AM_3X_5 - CsV_3Sb_5 obtained from diffraction measurements.

Element	Site	Formula	Solubility limit
Na	Na _{Cs}	Na _x Cs _{1-x} V ₃ Sb ₅	$x:[0,0.2]$
K	K _{Cs}	K _x Cs _{1-x} V ₃ Sb ₅	$x:[0,1.0]$
Rb	Rb _{Cs}	Rb _x Cs _{1-x} V ₃ Sb ₅	$x:[0,1.0]$
As	As _{Sb}	CsV ₃ Sb _{5-x} As _x	$x:[0,0.3]$
Bi	Bi _{Sb}	CsV ₃ Sb _{5-x} Bi _x	$x:[0,0.4]$
Nb	Nb _V	CsV _{3-x} Nb _x Sb ₅	$x:[0,0.2]$
Ta	Ta _V	CsV _{3-x} Ta _x Sb ₅	$x:[0,0.1]$

the sample stage using a small quantity of cigarette paper and GE varnish to ensure electrical isolation and thermal contact. Samples were then exfoliated and contacts established using silver paint (DuPont cp4929N-100) and gold wire (Alfa Aesar, 0.05-mm premium 99.995%). We used a probe current of 1 mA and frequency ≈ 100 Hz to measure the onset of superconductivity under zero-field conditions.

III. POLYCRYSTALLINE RESULTS AND DISCUSSION

Polycrystalline samples can be made quickly and with precise control over stoichiometry, providing an efficient means of traversing potential alloy spaces. Although this paper will explicitly focus on alloys among KV_3Sb_5 , RbV_3Sb_5 , and

CsV_3Sb_5 , we note here that we also performed a cursory exploration of other isoelectronic alloys with CsV_3Sb_5 . We explored Bi_{Sb}, As_{Sb}, Nb_V, Ta_V, and Na_{Cs}. A summary of the solubility limits as determined by diffraction is shown in Table I. None of the above produced new AM_3X_5 compounds, and attempts to alloy the individual components within CsV_3Sb_5 resulted in relatively low solubility. This was somewhat unexpected, considering that some electronically active dopants have exhibited extensive solubility (e.g., Sn_{Sb} reaches nearly CsV_3Sb_4Sn [27]). We explored other isoelectronic combinations with Tl⁺, Au⁺, and Hg⁺, although no new variants emerged.

Now turning to the synthesis and characterization of AV_3Sb_5 alloys within the KV_3Sb_5 - RbV_3Sb_5 - CsV_3Sb_5 phase space, Figures 2(a) and 2(b) shows the resulting cell volume of the AV_3Sb_5 structure as a function of composition throughout the entire KV_3Sb_5 - RbV_3Sb_5 - CsV_3Sb_5 phase diagram. Figure 2(a) clearly highlights the continuous change in cell volume among the three end members as would be expected for a full-solid solution. In Fig. 2(b), an alternate depiction of Fig. 2(a) is shown where the x axis is recast as the *theoretical cell volume* under the auspice of Vegard's law (linear interpolation of the lattice parameters of pure KV_3Sb_5 , RbV_3Sb_5 , and CsV_3Sb_5 powders). The parent compositions have been highlighted for reference, and a 1:1 correspondence is drawn as a gray line. The close agreement of the volume in Fig. 2(b)

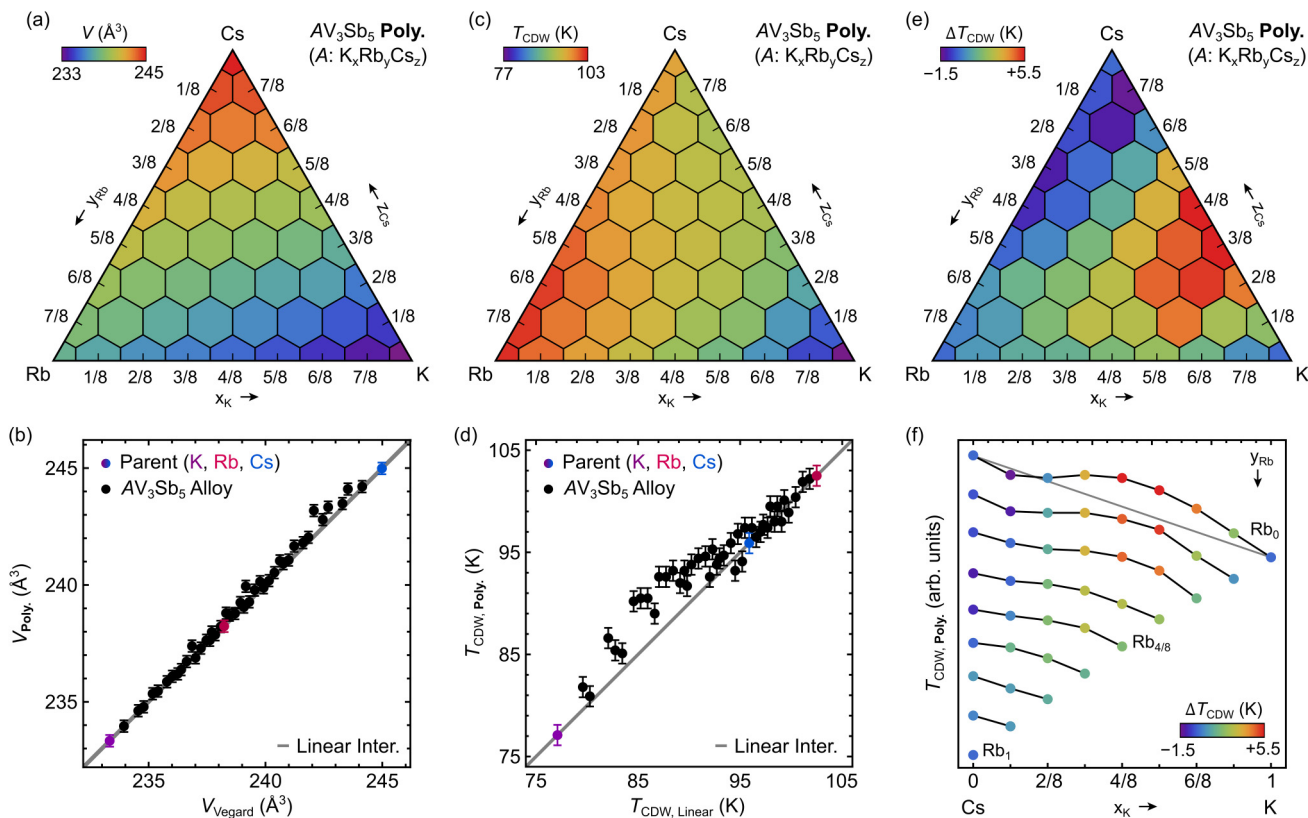


FIG. 2. Experimental synthesis of AV_3Sb_5 polycrystalline alloys (a) and (b) reveals a full solid solution among the three parent compounds that obeys linear interpolation (e.g., Vegard's law). The charge-density wave temperature T_{CDW} also trends smoothly between the termini (c), although the trends are not strictly linear (d). A plot of ΔT_{CDW} as a function of composition reveals a pocket of enhanced T_{CDW} along the $K_{1-x}Cs_xV_3Sb_5$ alloy line which is smooth and continuous (e). Note that the curves in (f) are offset for visual clarity, although the scales of the curves are consistent.

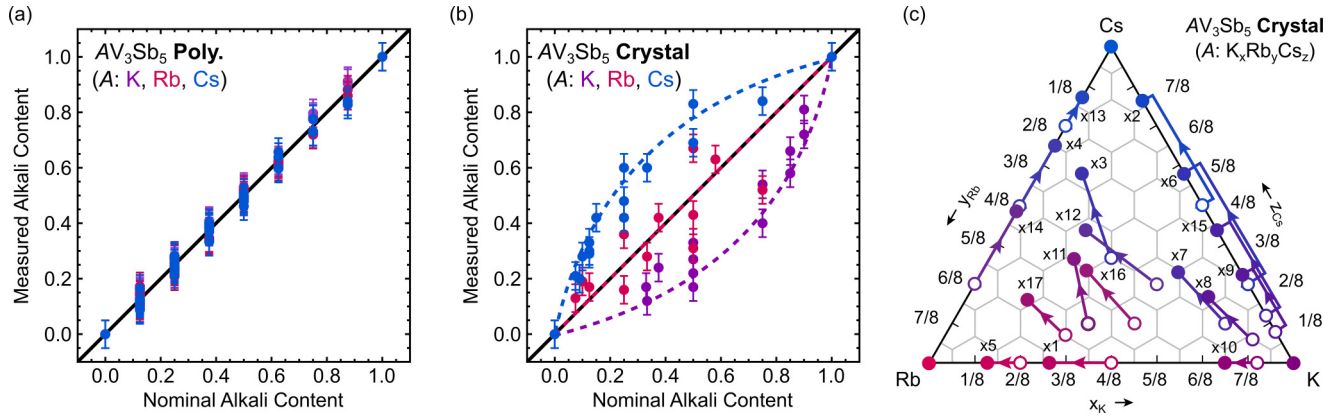


FIG. 3. Here we compare compositional control in polycrystalline and single-crystal samples of AV_3Sb_5 alloys. EDS on polycrystalline samples (a) highlights that all samples exhibit alkali-metal ratios consistent with their nominal loading. Single-crystal samples (b), however, exhibit alkali-metal content that deviates from their nominal values. We observe that (K, Rb, and Cs) mixtures tend to be deficient in K and exhibit excess Cs. These relationships can be visualized as a vector map (c) in the KV_3Sb_5 – RbV_3Sb_5 – CsV_3Sb_5 space, highlighting the “loss vector.” Although empirical, this provides a means to target a given AV_3Sb_5 composition.

with the linear projection indicates excellent agreement with Vegard’s law and confirms that the entire AV_3Sb_5 family exists as a single solid solution.

It is worth highlighting the consequence of the AV_3Sb_5 single solid solution. This indicates that KV_3Sb_5 , RbV_3Sb_5 , and CsV_3Sb_5 are not line compounds, but terminal ends of a full solid solution in a three-dimensional phase space. The continuous chemical alloying also presents an opportunity to investigate chemical-property changes throughout the AV_3Sb_5 family. Properties attributed as unique to CsV_3Sb_5 may exhibit interesting “crossover” points as we alloy with other end points. For example, as a potential future study, the incremental addition of Rb or K into CsV_3Sb_5 may help illuminate the nature of the $2 \times 2 \times 4$ CDW order which is only reported in CsV_3Sb_5 [18–20].

Having established that a solid solution is possible, we next turn to evolution of the CDW state across the series of AV_3Sb_5 alloy powders. Figure 2(c) shows a heat map of the CDW temperature T_{CDW} as a function of alloying composition. For a consistent, unbiased extraction of T_{CDW} from the magnetization data, T_{CDW} is defined as the peak in the derivative $d(MT)/dT$. A clear continuous gradient among the three parent compounds is observed, although Fig. 2(c) disguises some nuances in T_{CDW} as a function of composition. Figure 2(d) shows the T_{CDW} with the x axis again recast as the *theoretical* T_{CDW} if we presume a simple linear interpolation among the three parent compositions. Again we highlight the three pure parent compositions on the graph. The data near RbV_3Sb_5 agrees well with a linear interpretation; however, substantial deviations from nominal values are revealed as the transition towards KV_3Sb_5 is approached.

Further exploring this departure, Fig. 2(e) transforms the data from Figs. 2(c) and 2(d) as ΔT_{CDW} , where $\Delta T_{CDW} = T_{CDW} - T_{CDW,Linear}$. This allows the deviation from linearity in T_{CDW} to be visualized as a function of composition. The most prominent feature occurs along the $K_{1-x}Cs_xV_3Sb_5$ series of alloys where we observe a substantial enhancement of the CDW above the nominal (linearly interpolated) value. Figure 2(f) plots one-dimensional slices through the ΔT_{CDW} data, allowing an alternate perspective. Each curve connected

by black is a iso-Rb composition, demonstrating the change in T_{CDW} as a function of the K:Cs ratio. The gray line on the Rb_0 contour is the result from linear interpolation, and the color scheme is true to ΔT_{CDW} . The iso-Rb contours are offset graphically in the y direction for visual clarity. Interestingly, if one was to continuously grade a composition from CsV_3Sb_5 – RbV_3Sb_5 , and then from RbV_3Sb_5 – KV_3Sb_5 , the trends in T_{CDW} are nearly linear, suggesting that something unique may happen between K:Cs mixtures where a pocket of “enhanced” T_{CDW} can be observed along the $K_{1-x}Cs_xV_3Sb_5$ line.

We now turn to analysis of how the superconducting transition evolves across the phase diagram. In prior studies, polycrystalline samples and single crystals have always shown reasonable agreement with onset temperature of the CDW state in AV_3Sb_5 . However, the superconducting transition can be seemingly degraded by disorder/strain effects native to powders. For instance, powder samples require an additional annealing step to obtain fully superconducting volume fractions [2,27,28]. This is likely due to powders exhibiting an enhanced sensitivity to strain and deformation where even slight grinding in an agate mortar and pestle is sufficient to suppress the superconducting state. Prior to annealing, such powders remain highly crystalline by XRD and the CDW is unaffected—making powders nonideal for measurement of the superconductivity. As a result, we also created a smaller set of single-crystal samples to explore the evolution of superconductivity in tandem to the CDW state across the AV_3Sb_5 alloy space.

IV. SINGLE-CRYSTAL RESULTS AND DISCUSSION

A series of 20 single crystals of varying target compositions were grown, and Fig. 3 compares the resulting compositional control in polycrystalline samples versus single crystals. Figure 3(a) shows the experimentally measured alkali content in the 45 polycrystalline samples shown in Fig. 1 as a function of their *nominal* composition. All powder samples fall within the standard error of EDS chemical composition measurements. However, flux-grown crystals of AV_3Sb_5

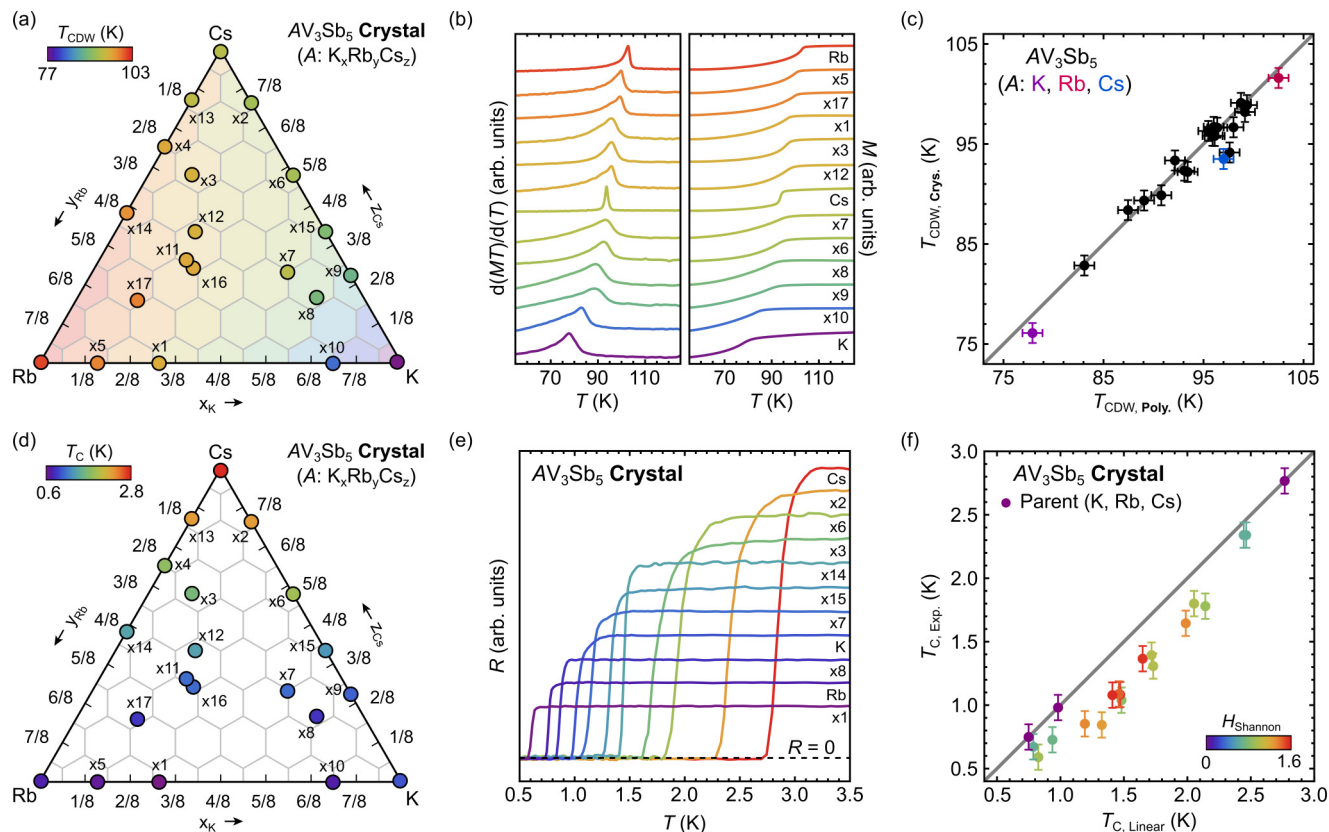


FIG. 4. Here we examine the charge-density wave and superconducting transitions in 20 unique single-crystal AV₃Sb₅ samples (17 alloys). The T_{CDW} (a) data extracted using the peak in the $d(MT)/dT$ data, (b) is shown superimposed with the polycrystalline data. Note that $d(MT)/dT$ data and $M(T)$ is shown in arb. units and has been scaled and offset for visual comparison. Excellent agreement between the polycrystalline (interpolated experimental T_{CDW} surface) and the single-crystal T_{CDW} data (c) indicates that the crystals exhibit the same trends—and that the polycrystalline data can serve as a good proxy for selecting compositions. Analogous superconducting transitions (d) are extracted using the zero-resistivity condition in transport data (e). Note that resistivity curves are shown in arb. units and have been scaled for visual clarity. In all cases we observe a suppression of T_c relative to a naive linear interpolation (f), consistent with the effect of chemical disorder.

show substantially more complex behavior. Figure 3(b) shows the compositional data for the 20 single-crystal samples (3 parents, 17 alloys). *Relative to their nominal compositions*, samples that include K are always deficient in K. The opposite is observed for Cs, which is always more abundant than the nominal content. Interestingly, the *ratio* of Rb to the other elements appears to be largely consistent with the nominal target composition.

Figure 3(c) provides an alternate way to visualize compositional trends in the flux grown crystals. Open circles highlight starting “nominal” compositions, whereas the closed circles indicate the final “measured” composition. The compositional vector is referred to as the loss vector and can be used to map nominal alkali loading onto the expected composition. Several qualitative rules can be inferred: (1) In (K, Rb, Cs)V₃Sb₅ mixtures, relative abundance trends towards the Rb:Cs edge of the diagram, (2) In pairwise mixtures with Cs, the Cs will always exist in relative abundance relative to the target composition, and (3) In pairwise mixtures, K will always exist in relative scarcity relative to the target composition.

The difference between the nominal and measured compositions are relatively large for many compositions. Speculat-

ing, we suspect that mixtures of the three AV₃Sb₅ compounds likely modify the melting point of the fluxes substantially and change the relative stability and constituent chemical potentials of the various alkali metals. However, the loss vectors shown in Fig. 3(c) are relatively consistent in length and direction, allowing specific compositions to be targeted empirically, even without more intimate knowledge of the liquidus surface and melting points. We note here that *within* a given AV₃Sb₅ alloy batch, a random selection of >5 crystals all exhibit consistent compositions. This implies that a given flux composition yields reproducible and homogeneous conditions within the growth.

The single-crystal samples presented in Fig. 3 provide another platform to explore the connection between the A-site chemistry and the CDW state. Figure 4(a) shows T_{CDW} as a function of composition, again extracted using the peak in $d(MT)/dT$. The powder data has been included as a transparent background to show qualitative agreement with the prior polycrystalline data. A representative selection of the $d(MT)/dT$ curves and the raw magnetization data are also shown in Fig. 4(b) for comparison. For clarity we have included all single-crystal magnetization results in the Supplemental Material [41]. Alloyed single crystals tend to exhibit

broader T_{CDW} transitions, although not substantially broader than the transition in pure KV_3Sb_5 .

Recall that one of the unique features of the polycrystalline T_{CDW} data in Fig. 2 was the dome of enhanced T_{CDW} relative to the linear interpolation. Due to the limitations of single-crystal synthesis (largely a throughput issue), the single-crystal data in Fig. 4(a) can be considered “aliased.” Figure 4(c) harmonizes the single-crystal and polycrystalline data to determine whether we expect single-crystal alloys along $\text{K}_{1-x}\text{Cs}_x\text{V}_3\text{Sb}_5$ to exhibit analogous trends. Here we show the experimentally extracted T_{CDW} for single crystals against the *interpolated* $T_{\text{CDW, Poly}}$ for powders. Note that the *interpolated* $T_{\text{CDW, Poly}}$ is not a linear interpolation, but a learned interpolation based on the experimental surface observed in Figs. 2(c)–2(f). The 1:1 agreement in Fig. 4(c) highlights that the single-crystal data is in excellent agreement with the polycrystalline data. Thus, the polycrystalline data can serve as a proxy to identify interesting compositions, which can be subsequently targeted using the vector map in Fig. 3(c). As one exception to this, the points exhibiting largest deviation from the 1:1, crystal:powder correspondence are pure CsV_3Sb_5 and a Cs-rich crystal. Deviations between the CDW temperatures in powders and single crystals of pure CsV_3Sb_5 were reported earlier [2,27], and the origin for this difference remains an open question.

Next we examine the effect of *A*-site alloying on the superconducting transitions of AV_3Sb_5 alloys. Figure 4(d) shows a heat map of the single-crystal samples and their respective T_c , extracted from resistivity measurements at low temperatures. Figure 4(e) shows a selection of the raw resistivity curves for comparison. As with the magnetization results, all resistivity results on single crystals have been included in the Supplemental Material [41]. As a conservative estimate, we use the zero-resistivity condition to define T_c . In doing so, the T_c 's of the parent compounds agree with published heat-capacity and Meissner state data within 0.2 K. Note that the initial report of superconductivity in RbV_3Sb_5 lists T_c as 0.92 K [4], although the zero-resistivity condition in that paper is 0.75 K, in agreement with our current data.

Figure 4(f) compares T_c for the AV_3Sb_5 alloys with a simple linear interpolation between the three parent compounds. All alloys exhibit T_c values that are suppressed relative to the parent KV_3Sb_5 , RbV_3Sb_5 , and CsV_3Sb_5 compounds. All samples also maintain a clear superconducting transition and zero resistivity state. To verify the bulk nature of the transition in the alloyed compositions, we performed heat-capacity

measurements on a heavily alloyed single crystal [41], confirming that the bulk nature of the superconducting state. The global suppression of T_c is consistent with the influence of increased chemical and site disorder induced by *A*-site alloying. As means of further visualizing this, the data points in Fig. 4(f) are color coded using the Shannon entropy, calculated as $H = -\sum_{i=3}^n p(x_i) \log_b p(x_i)$. Here the probabilities $p(x_i)$ are approximated as the relative concentration of the three alkali metals measured in each crystal. As a general trend, samples with higher entropy mixtures (e.g., closest to 1:1:1 K:Rb:Cs) show the largest suppression of T_c , consistent with the role of disorder.

V. CONCLUSION

In this paper, we investigated alloys of the AV_3Sb_5 kagome superconductors using both polycrystalline and single-crystal samples. We identified that KV_3Sb_5 , RbV_3Sb_5 , and CsV_3Sb_5 share a full solid solution, with full miscibility on the alkali site. This provides a conceptual shift, wherein the AV_3Sb_5 materials can be viewed as a continuum with the three “parent” structures as the terminal ends of a single phase space. We presented the means to design AV_3Sb_5 single-crystal alloys of desired compositions, and explored the charge-density wave (T_{CDW}) and superconducting temperatures (T_c) as a function of *A*-site composition. In contrast to the linear trends seen in the structural properties (e.g., cell volume), we observed continuous *nonlinear* changes in T_c and T_{CDW} . For example, we identified a small dome of enhanced CDW stability along alloys of $\text{K}_{1-x}\text{Cs}_x\text{V}_3\text{Sb}_5$. By dramatically expanding the available chemical space, this paper provides a new materials-based route for probing the rich electronic phase diagram of the AV_3Sb_5 kagome superconductors.

ACKNOWLEDGMENTS

This work was supported by the National Science Foundation (NSF) through Enabling Quantum Leap: Convergent Accelerated Discovery Foundries for Quantum Materials Science, Engineering and Information (Q-AMASE-i): Quantum Foundry at UC Santa Barbara (Grant No. DMR-1906325). The research made use of the shared experimental facilities of the NSF Materials Research Science and Engineering Center at UC Santa Barbara (Grant No. DMR-1720256). The UC Santa Barbara MRSEC is a member of the Materials Research Facilities Network [42].

-
- [1] B. R. Ortiz, L. C. Gomes, J. R. Morey, M. Winiarski, M. Bordelon, J. S. Mangum, I. W. H. Oswald, J. A. Rodriguez-Rivera, J. R. Neilson, S. D. Wilson, E. Ertekin, T. M. McQueen, and E. S. Toberer, New kagome prototype materials: discovery of KV_3Sb_5 , RbV_3Sb_5 , and CsV_3Sb_5 , *Phys. Rev. Mater.* **3**, 094407 (2019).
- [2] B. R. Ortiz, S. M. L. Teicher, Y. Hu, J. L. Zuo, P. M. Sarte, E. C. Schueller, A. M. M. Abeykoon, M. J. Krogstad, S. Rosenkranz, R. Osborn, R. Seshadri, L. Balents, J. He, and S. D. Wilson, CsV_3Sb_5 : A \mathbb{Z}_2 Topological Kagome Metal with

a Superconducting Ground State, *Phys. Rev. Lett.* **125**, 247002 (2020).

- [3] B. R. Ortiz, P. M. Sarte, E. M. Kenney, M. J. Graf, S. M. L. Teicher, R. Seshadri, and S. D. Wilson, Superconductivity in the \mathbb{Z}_2 kagome metal KV_3Sb_5 , *Phys. Rev. Mater.* **5**, 034801 (2021).
- [4] Q. Yin, Z. Tu, C. Gong, Y. Fu, S. Yan, and H. Lei, Superconductivity and normal-state properties of kagome metal RBV_3Sb_5 single crystals, *Chin. Phys. Lett.* **38**, 037403 (2021).
- [5] H. Chen, H. Yang, B. Hu, Z. Zhao, J. Yuan, Y. Xing, G. Qian, Z. Huang, G. Li, Y. Ye *et al.*, Roton pair density wave in a

- strong-coupling kagome superconductor, *Nature (London)* **599**, 222 (2021).
- [6] J. Ge, P. Wang, Y. Xing, Q. Yin, H. Lei, Z. Wang, and J. Wang, Discovery of charge-4e and charge-6e superconductivity in kagome superconductor CsV_3Sb_5 , [arXiv:2201.10352](https://arxiv.org/abs/2201.10352).
- [7] Y. Xu, Z. Ni, Y. Liu, B. R. Ortiz, S. D. Wilson, B. Yan, L. Balents, and L. Wu, Universal three-state nematicity and magneto-optical Kerr effect in the charge density waves in AV_3Sb_5 ($A = Cs, Rb, K$), *Nat. Phys.* **18**, 1470 (2022).
- [8] C. Mielke III, D. Das, J.-X. Yin, H. Liu, R. Gupta, Y.-X. Jiang, M. Medarde, X. Wu, H. Lei, J. Chang *et al.*, Time-reversal symmetry-breaking charge order in a kagome superconductor, *Nature (London)* **602**, 245 (2022).
- [9] L. Yu, C. Wang, Y. Zhang, M. Sander, S. Ni, Z. Lu, S. Ma, Z. Wang, Z. Zhao, H. Chen *et al.*, Evidence of a hidden flux phase in the topological kagome metal CsV_3Sb_5 , [arXiv:2107.10714](https://arxiv.org/abs/2107.10714).
- [10] C. Guo, C. Putzke, S. Konyzheva, X. Huang, M. Gutierrez-Amigo, I. Errea, D. Chen, M. G. Vergniory, C. Felser, M. H. Fischer *et al.*, Switchable chiral transport in charge-ordered kagome metal CsV_3Sb_5 , *Nature (London)*, 461 (2022).
- [11] Y.-X. Jiang, J.-X. Yin, M. M. Denner, N. Shumiya, B. R. Ortiz, G. Xu, Z. Guguchia, J. He, M. S. Hossain, X. Liu *et al.*, Unconventional chiral charge order in kagome superconductor KV_3Sb_5 , *Nature Mater.* **20**, 1353 (2021).
- [12] Y. Hu, S. M. Teicher, B. R. Ortiz, Y. Luo, S. Peng, L. Huai, J. Ma, N. C. Plumb, S. D. Wilson, J. He *et al.*, Topological surface states and flat bands in the kagome superconductor CsV_3Sb_5 , *Sci. Bull.* **67**, 495 (2022).
- [13] M. Kang, S. Fang, J.-K. Kim, B. R. Ortiz, S. H. Ryu, J. Kim, J. Yoo, G. Sangiovanni, D. Di Sante, B.-G. Park *et al.*, Twofold van Hove singularity and origin of charge order in topological kagome superconductor CsV_3Sb_5 , *Nat. Phys.* **18**, 301 (2022).
- [14] Y. Hu, X. Wu, B. R. Ortiz, S. Ju, X. Han, J. Ma, N. C. Plumb, M. Radovic, R. Thomale, S. D. Wilson *et al.*, Rich nature of Van Hove singularities in Kagome superconductor CsV_3Sb_5 , *Nat. Commun.* **13**, 2220 (2022).
- [15] H. Tan, Y. Liu, Z. Wang, and B. Yan, Charge Density Waves and Electronic Properties of Superconducting Kagome Metals, *Phys. Rev. Lett.* **127**, 046401 (2021).
- [16] M. M. Denner, R. Thomale, and T. Neupert, Analysis of Charge Order in the Kagome Metal AV_3Sb_5 ($a = K, Rb, Cs$), *Phys. Rev. Lett.* **127**, 217601 (2021).
- [17] M. H. Christensen, T. Birol, B. M. Andersen, and R. M. Fernandes, Theory of the charge density wave in AV_3Sb_5 kagome metals, *Phys. Rev. B* **104**, 214513 (2021).
- [18] B. R. Ortiz, S. M. L. Teicher, L. Kautzsch, P. M. Sarte, N. Ratcliff, J. Harter, J. P. C. Ruff, R. Seshadri, and S. D. Wilson, Fermi Surface Mapping and the Nature of Charge-Density-Wave Order in the Kagome Superconductor CsV_3Sb_5 , *Phys. Rev. X* **11**, 041030 (2021).
- [19] Y. Hu, X. Wu, B. R. Ortiz, X. Han, N. C. Plumb, S. D. Wilson, A. P. Schnyder, and M. Shi, Coexistence of tri-hexagonal and star-of-david pattern in the charge density wave of the kagome superconductor AV_3Sb_5 , [arXiv:2201.06477](https://arxiv.org/abs/2201.06477).
- [20] M. Kang, S. Fang, J. Yoo, B. R. Ortiz, Y. Oey, S. H. Ryu, J. Kim, C. Jozwiak, A. Bostwick, E. Rotenberg *et al.*, Microscopic structure of three-dimensional charge order in kagome superconductor AV_3Sb_5 and its tunability, *Nature Mater.* (2022).
- [21] Q. Stahl, D. Chen, T. Ritschel, C. Shekhar, E. Sadrollahi, M. C. Rahn, O. Ivashko, M. v. Zimmermann, C. Felser, and J. Geck, Temperature-driven reorganization of electronic order in CsV_3Sb_5 , *Phys. Rev. B* **105**, 195136 (2022).
- [22] Q. Xiao, Y. Lin, Q. Li, W. Xia, X. Zheng, S. Zhang, Y. Guo, J. Feng, and Y. Peng, Coexistence of multiple stacking charge density waves in kagome superconductor CsV_3Sb_5 , [arXiv:2201.05211](https://arxiv.org/abs/2201.05211).
- [23] L. Kautzsch, Y. M. Oey, H. Li, Z. Ren, B. R. Ortiz, R. Seshadri, J. Ruff, Z. Wang, I. Zeljkovic, and S. D. Wilson, Incommensurate charge-stripe correlations in the kagome superconductor $CsV_3Sb_{5-x}Sn_x$, [arXiv:2207.10608](https://arxiv.org/abs/2207.10608).
- [24] H. Zhao, H. Li, B. R. Ortiz, S. M. Teicher, T. Park, M. Ye, Z. Wang, L. Balents, S. D. Wilson, and I. Zeljkovic, Cascade of correlated electron states in the kagome superconductor CsV_3Sb_5 , *Nature (London)* **599**, 216 (2021).
- [25] H. Li, H. Zhao, B. Ortiz, Y. Oey, Z. Wang, S. D. Wilson, and I. Zeljkovic, Emergence of unidirectional coherent quasiparticles from high-temperature rotational symmetry broken phase of AV_3Sb_5 kagome superconductors, [arXiv:2203.15057](https://arxiv.org/abs/2203.15057).
- [26] J. Yu, Z. Xu, K. Xiao, Y. Yuan, Q. Yin, Z. Hu, C. Gong, Y. Guo, Z. Tu, P. Tang *et al.*, Evolution of electronic structure in pristine and rb-reconstructed surfaces of kagome metal RbV_3Sb_5 , *Nano Lett.* **22**, 918 (2022).
- [27] Y. M. Oey, B. R. Ortiz, F. Kaboudvand, J. Frassinetti, E. Garcia, R. Cong, S. Sanna, V. F. Mitrović, R. Seshadri, and S. D. Wilson, Fermi level tuning and double-dome superconductivity in the kagome metal $CsV_3Sb_{5-x}Sn_x$, *Phys. Rev. Mater.* **6**, L041801 (2022).
- [28] Y. M. Oey, F. Kaboudvand, B. R. Ortiz, R. Seshadri, and S. D. Wilson, Tuning charge density wave order and superconductivity in the kagome metals $KV_3Sb_{5-x}Sb_x$ and $RbV_3Sb_{5-x}Sb_x$, *Phys. Rev. Mater.* **6**, 074802 (2022).
- [29] H. Yang, Z. Zhao, X.-W. Yi, J. Liu, J.-Y. You, Y. Zhang, H. Guo, X. Lin, C. Shen, H. Chen *et al.*, Titanium-based kagome superconductor $CsTi_3Bi_5$ and topological states, [arXiv:2209.03840](https://arxiv.org/abs/2209.03840).
- [30] Y. Liu, Y. Wang, Y. Cai, Z. Hao, X.-M. Ma, L. Wang, C. Liu, J. Chen, L. Zhou, J. Wang *et al.*, Doping evolution of superconductivity, charge order and band topology in hole-doped topological kagome superconductors $Cs(V_{1-x}Ti_x)_3Sb_5$, [arXiv:2110.12651](https://arxiv.org/abs/2110.12651).
- [31] Y. Li, Q. Li, X. Fan, J. Liu, Q. Feng, M. Liu, C. Wang, J.-X. Yin, J. Duan, X. Li *et al.*, Tuning the competition between superconductivity and charge order in the kagome superconductor $Cs(V_{1-x}Nb_x)_3Sb_5$, *Phys. Rev. B* **105**, L180507 (2022).
- [32] M. Liu, T. Han, X. Hu, Y. Tu, Z. Zhang, M. Long, X. Hou, Q. Mu, and L. Shan, Evolution of superconductivity and charge density wave through Ta and Mo doping in CsV_3Sb_5 , *Phys. Rev. B* **106**, L140501 (2022).
- [33] Y. Song, T. Ying, X. Chen, X. Han, X. Wu, A. P. Schnyder, Y. Huang, J.-g. Guo, and X. Chen, Competition of Superconductivity and Charge Density Wave in Selective Oxidized CsV_3Sb_5 Thin Flakes, *Phys. Rev. Lett.* **127**, 237001 (2021).
- [34] F. Du, S. Luo, B. R. Ortiz, Y. Chen, W. Duan, D. Zhang, X. Lu, S. D. Wilson, Y. Song, and H. Yuan, Pressure-induced double superconducting domes and charge instability in the kagome metal KV_3Sb_5 , *Phys. Rev. B* **103**, L220504 (2021).
- [35] K. Y. Chen, N. N. Wang, Q. W. Yin, Y. H. Gu, K. Jiang, Z. J. Tu, C. S. Gong, Y. Uwatoko, J. P. Sun, H. C. Lei, J. P. Hu, and J.-G. Cheng, Double Superconducting Dome and Triple

- Enhancement of T_c in the Kagome Superconductor CsV_3Sb_5 Under High Pressure, *Phys. Rev. Lett.* **126**, 247001 (2021).
- [36] C. C. Zhu, X. F. Yang, W. Xia, Q. W. Yin, L. S. Wang, C. C. Zhao, D. Z. Dai, C. P. Tu, B. Q. Song, Z. C. Tao, Z. J. Tu, C. S. Gong, H. C. Lei, Y. F. Guo, and S. Y. Li, Double-dome superconductivity under pressure in the V-based kagome metals AV_3Sb_5 ($A = \text{Rb}$ and K), *Phys. Rev. B* **105**, 094507 (2022).
- [37] F. H. Yu, D. H. Ma, W. Z. Zhuo, S. Q. Liu, X. K. Wen, B. Lei, J. J. Ying, and X. H. Chen, Unusual competition of superconductivity and charge-density-wave state in a compressed topological kagome metal, *Nat. Commun.* **12**, 1 (2021).
- [38] B. R. Ortiz, J. M. Adamczyk, K. Gordiz, T. Braden, and E. S. Toberer, Towards the high-throughput synthesis of bulk materials: thermoelectric $\text{PbTe-PbSe-SnTe-SnSe}$ alloys, *Mol. Syst. Des. Eng.* **4**, 407 (2019).
- [39] A. A. Coelho, *TOPAS* and *TOPAS-Academic*: an optimization program integrating computer algebra and crystallographic objects written in C++, *J. Appl. Crystallogr.* **51**, 210 (2018).
- [40] K. Momma and F. Izumi, *VESTA3* for three-dimensional visualization of crystal, volumetric and morphology data, *J. Appl. Crystallogr.* **44**, 1272 (2011).
- [41] See Supplemental Material at <http://link.aps.org/supplemental/10.1103/PhysRevMaterials.7.014801> for further details.
- [42] www.mrfn.org.